RSC Advances

ROYAL SOCIETY OF CHEMISTRY

www.rsc.org/advances

Low temperature magnetic and transport properties of LSMO-PZT nanocomposites

Gopeshwar Dhar Dwivedi,[+a] Manish Kumar,[a] Prashant Shahi,[b] Anjan Barman,[c] Sandip Chatterjee[b] and Anup K. Ghosh[*a]

[a] *Materials Research Laboratory, Department of Physics, Banaras Hindu University, Varanasi-221005, India*
[b] *Department of Physics, Indian Institute of Technology (BHU), Varanasi-221005, India*
[c] *Department of Material Sciences, S.N. Bose National Centre for Basic Sciences, Salt Lake, Kolkata-700 098, India.*

Abstract

Nanocomposites of $La_{0.7}Sr_{0.3}MnO_3$-$PbZr_{0.52}Ti_{0.48}O_3$ (LSMO-PZT) with varying PZT content have been synthesized by sol-gel method. The XRD, HRTEM, SEM and EDX studies confirm the coexistence of both the components (viz. LSMO and PZT) in the composites and reveal that the PZT nanoparticles occupy the surface and the grain boundaries (GBs). The M–H measurement of LSMO-PZT composites exhibits weak ferromagnetic nature with low coercivity of 0.0123 T and 0.0142 T at 300 K and 80 K respectively and the highest magnetic moment (n_B) achieved is 2.069 μ_B at 80 K for x=0.01. The M-T studies confirm the transition temperature (T_c) ≈ 360 K and the maximum entropy changes (ΔS_m) are 0.40, 0.35 and 0.25 $mJKg^{-1}K^{-1}$ at the magnetic field H_{max}=100 Oe for x=0.01, 0.02 and 0.05 respectively. The average particle size of LSMO, PZT, and LSMO-PZT nanocomposites ranges between 24 nm - 30 nm, as confirmed from XRD, TEM, and magnetic measurements. Electrical resistivity studies show that the insulator–metal transition temperature (T_{IM}) decreases rapidly with addition of small amount of PZT and then remains almost constant with higher concentration of PZT. The conduction in the insulator region is governed by tunneling between magnetic phases and in the metallic region the conduction shows non-Fermi liquid behavior. The resistivity increases with increasing PZT concentration. The energy barriers and scatterings are responsible for increase in higher resistivity observed. The magneto-resistance (%MR) has been found to decrease with decreasing temperature. Variation in the MR at low temperature in LSMO-PZT nanocomposite is due to the effect of the large spin polarization and pinning of domain walls at the GBs.

Key words: Nanomaterials, Nanocomposites, Structural properties, Magnetic properties, electrical transport properties, Magneto-resistance.

* Correspondence should be addressed to: akghosh@bhu.ac.in (Anup K. Ghosh).

+ Present address: National Sun Yat-Sen University, Kaohsiung, Taiwan

Introduction

Mixed valence perovskite oxides ($R_{1-x}A_xMO_3$, where R, A, and M are trivalent rare earth cations, divalent alkaline-earth cations, and transition metal cations, respectively) have attracted great interest due to their rich varieties of interesting properties such as spin-, orbital- and charge- ordering, giant magnetoresistance, colossal magnetoresistance (CMR), phase separation and metal–insulator transitions etc.[1-4]. The interplay of different types of ordering and different degrees of freedom takes a very important role in determining the properties of such strongly correlated electron systems. The large variation in the carrier mobility originates from an insulator-metal transition is closely associated with the magnetic ordering. When trivalent rare-earth La ions at the A-site are partially substituted with divalent alkaline-earth elements such as Ca, Ba, Sr, Pb, etc. in $LaMnO_3$ (with formula ABO_3) mixed valencies of the manganese ions in the B-site (Mn^{3+}–Mn^{4+}) are created and significant increase in the electrical conductivity and magnetization of the compound occur due to double exchange mechanism.[2–4] Among these perovskite manganites, $La_{1-x}Sr_xMnO_3$ (also called half-metallic ferromagnetic materials) exhibits strong ferromagnetism, metallic conductivity, tuned transition temperature (T_c) and many other properties. It is especially interesting due to the fact that its Curie temperature (T_c) is the highest in the concentration range where colossal magnetoresistance takes place. It is clear from the phase diagram showing the magnetic and metal-insulator transitions[5,6] that the electrical and magnetic properties of pure $LaMnO_3$ change strongly with Sr doping, which introduces holes in the manganese e_g band (Mn^{3+}/Mn^{4+} mixed valence state), eventually producing mobile charge carriers *i.e.* conduction and canting of Mn spins.[7–12] The low temperature phase of the pure and lightly doped samples ($x < 0.1$) is anti-ferromagnetic insulator, becomes a ferromagnetic insulator in the range $0.10 \leq x<0.16$, above which the insulator changes to metallic. For the end members of the dilution series, $LaMnO_3$ and $SrMnO_3$, the ground state is anti-ferromagnetic (AF), for spins interacting via the superexchange interaction[12] when the metal–oxygen–metal bond angle is close to 180°. In $SrMnO_3$ cubic perovskite internal

stresses arising from the mismatch between the equilibrium bond lengths Sr-O and Mn-O are relieved by a cooperative rotation of the MnO_6 octahedra that lowers the symmetry of the unit cell from cubic to rhombohedral (*R3c*) or orthorhombic (*Pbnm*).[13] The resultant bending of the Mn-O-Mn bond reduces the angle from 180° and reduces the σ-bonding. Origin of ferromagnetism, close correlation between magnetic and transport properties in $La_{0.7}Sr_{0.3}MnO_3$ (LSMO) had been explained on the basis of joint effects of double exchange interaction mechanism, strong electron-phonon interaction arising from the Jahn-Teller (JT) splitting of the outer Mn*d* level,[14,15] and grain boundary (GB) effects. In double exchange interaction model, the antiferromagnetic phase is progressively destroyed by the ferromagnetic coupling induced by the hopping of the e_g electron from a Mn^{3+} ion to the corresponding hole of a neighboring Mn^{4+} [Ref. 7–9] Strong Hund's rule coupling enhances the hopping of e_g electrons between neighboring Mn^{3+} and Mn^{4+} ions thereby producing a ferromagnetic interaction.[11] Cations of different size occupied in A-sites can produce a Jahn-Teller distortion of the MnO_6 octahedron. In addition to the double exchange interaction, a polaron effect due to a very strong electron-phonon coupling arising from a Jahn-Teller splitting of Mn^{3+} ion was proposed to explain the metal-insulator transition and corresponding CMR properties.[14,15] Most importantly, the average A-cation radius $<r_A>$ is the key parameter to affect the magnetoresistance, irrespective of the individual rare earth element.[16] Very recently Straumal et al. and others showed that the grain boundary (GB) and the grain boundary specific area (S_{GB}), defined as the GB area per unit grain volume, is the controlling factor for the ferromagnetic behavior of undoped and TM-doped ZnO.[17,18] The increase in MR in LSMO has been explained by assuming an increase of the grain boundary contribution.[19] The bulk $La_{0.7}Sr_{0.3}MnO_3$ (LSMO) is of great interest, since it possesses the highest value of the metal-insulator transition and ferromagnetic transition simultaneously at around 370 K[5] and combines low carrier density (10^{21}–$10^{22}cm^3$) with a high spin polarization of charge carriers[20] among perovskite-type $R_{1-x}A_xMO_3$ manganite systems.Bulk LSMO manifests very high value of colossal magnetoresistance (CMR), which can be utilized in the high sensitive sensors of magnetic field.[21] The interaction between pairs of Mn^{3+} and Mn^{4+} ions through an oxygen atom is responsible for the metal to insulator transition in the $La_{0.7}Sr_{0.3}MnO_3$. Since the electrical and magnetic properties strongly depend on particle size, several attempts have been made to prepare LSMO nanoparticles.[19,22,23] A large magnetic moment at room

temperature allows these manganite nanoparticles coated with appropriate macromolecules for biomedical applications including magnetic hyperthermia, because of their super-paramagnetic behavior. Tunable T_c also allow in marker experiments in bio-detection at the same time.[24–26] On the other hand, due to significant magneto-resistance effects at T_c, eddy currents can be utilized as part of the heating mechanism. Hence, one can achieve the selective heating of the given area of an organism by T_c-limiting production of controlled heating effects by means of an alternating external magnetic field.[27] Though, in bulk LSMO, metal-insulator transition and ferromagnetic transition occurs simultaneously at the same temperature, in nanophasic $La_{0.7}Sr_{0.3}MnO_3$ both transition occurs at different temperatures and these values depend on sintering temperatures.[19] Ferromagnetic transition temperature decreases slightly with decreasing sintering temperature but metal-insulator transition decreases significantly with decreasing sintering temperature.[19]

It is well known that crystalline $PbZr_{0.52}Ti_{0.48}O_3$ (PZT) is an insulting oxide with perovskite structure which is near the morphotropic phase boundary (MPB) between the rhombohedral Zr-rich phase and tetragonal Ti-rich phase, exhibits the maximum dielectric, piezoelectric and electromechanical constants along with a high ferroelectric Curie transition temperature of (350°C). It has been extensively studied and used for the applications of ultrasonic transducers, actuators, filters, resonators and detectors.[28–31]

Composites of ferromagnetic and ferroelectric compounds have attracted considerable interest because of their interesting and potential applications.[32,33] The coupling between electric and magnetic orderings called the magnetoelectric (ME) coupling in these materials is interesting. The magnetic, transport and magnetoelectric (ME) properties have immense importance for device applications. That is why in this paper we concentrate on the (LSMO-PZT) nanocomposites because a clear understanding of finite size effects is essential for the development of high-density magnetic storage media with nano-sized constituent particles. In present work, nanosized (1-x)LSMO-(x)PZT($0.01 \leq x \leq 0.05$) ceramics were prepared using sol-gel method. In this paper, structural, low temperature magnetic and transport properties of LSMO-PZT composites have been studied. However, the multiferroic properties viz., magnetic, ferroelectric, magneto-dielectric and ME coupling are currently under investigations and will be reported somewhere else.

Experimental procedure

$La_{0.7}Sr_{0.3}MnO_3$ (LSMO) nanoparticles were synthesized using sol-gel technique. $La(NO_3)_3.6H_2O$, $Sr(NO_3)_2$, and $Mn(NO_3)_2.6H_2O$ were taken in stoichiometric amounts and dissolved in distilled water under continuous stirring. Citric acid (CA) and ethylene glycol (EG) were added as complexation and polymerization agents, respectively. EG, CA and metal ions were taken in 4:3:1 mol ratio respectively. Obtained clear solution was heated on a hot plate at 80 °C to evaporate excess solvent and it turned into yellowish gel. The gel was further heated and dried at 200 °C to remove the organic parts. Then the gel turned into foam, which was dried again to decompose at 400 °C in furnace. The obtained precursor was ground into powder by an agate mortar and was calcined at 600 °C in air atmosphere for 10 hrs. Calcined powder was then further heat treated at 800 °C for 12 hrs.

$PbZr_{0.52}Ti_{0.48}O_3$ (PZT) nanoparticles (NP) were prepared using lead acetate trihydrate [$Pb(CH_3COO)_2.3H_2O$], titanium isopropoxide [$Ti(OCH(CH_3)_2)_4$], Zirconium n-propoxide [$Zr(OCH_2CH_2CH_3)_4$], 70% L-propanol, and 2-methoxyethanol ($CH_3OC_2H_4OH$) as the starting materials to prepare the precursor solutions for PZT NP. The atomic ratio of the Pb:Zr:Ti of the solution was 1:0.52:0.48. 10% excess lead acetate was introduced. Stoichiometric amounts of Lead acetate and Zirconium n-propoxide were dissolved in 2-methoxyethanol under stirring at room temperature separately. Required amount of titanium isopropoxide was then added to the Zirconium solution with addition of some small amount of solvent under stirring to prepare Zr-Ti solution. While stirring the Zr-Ti solution, Pb solution was added into it and heated at 60 °C for 30 minutes. The pH of the solution was adjusted to 5 by adding some water. After few minutes the color of the solution becomes milky white and becomes gelatinous. The gel was heated at 60 °C for 48 hrs and then calcined at 700 °C for 1 hr to get PZT powders.

1%, 2% and 5% of PZT nanoparticles were mixed with 99%, 98% and 95% LSMO nanoparticles respectively. Samples have been named according to the percentage of PZT present in the composite such as LP0 (pure LSMO), LP1 (1% PZT), LP2 (2% PZT) and LP5 (5% PZT). All the samples were then pelletized and heat treated at 700 °C for 2 hrs. X-ray diffraction has been done by Rigaku Miniflex II DEXTOP X-ray diffractometer with Cu-Kα radiation. Transmission Electron Microscopy (TEM) measurements have been carried out with JEOL-2010 (Japan). Magnetic measurements were taken using

Vibrating Sample Magnetometer (Lakeshore: Model no. 7407). Transport property measurements have been done by four probe method using Keithley 2182A nano-voltmeter and Keithley 2400 source meter.

Results and discussion

Fig. 1 shows the Rietveld refinement of the powder X-ray diffraction (XRD) patterns for pure and composite samples (LP0, LP1, LP2, LP5 and PZT). The peak positions of LP0 correspond to the standard Bragg positions of perovskite LSMO (rhombohedral; space group $R\bar{3}c$), which have been shown by the vertical bars and the residue by the line, respectively at the bottom of the XRD patterns as shown in Fig. 1(a). The powder X-ray diffraction patterns also confirm that there is no appearance of any extra peaks or disappearance of any peak of the rhombohedral structure of pure LSMO and the sample LP0 is of single phase. Miller indices (*hkl*) of the diffraction peaks of LSMO and PZT are matched with JCPDS card numbers 00-051–0409 and 33–0784 respectively. The powder X-ray diffraction patterns for pure PZT refined with space group *P4mm* is shown in Fig. 1(b). The powder X-ray diffraction patterns of LP1, LP2 and LP5 nanocomposites have been refined with space group ($R\bar{3}c$ + *P4mm*). The peak positions of all composites correspond to the standard Bragg positions of perovskite LSMO have been shown by the lower vertical bars, Bragg positions of PZT by the upper vertical bars and the residue by the line, respectively at the bottom of the XRD patterns as shown in Fig. 1(a). Closer look of the XRD patterns (Fig. 1(a)) shows the presence of PZT in LP5 composite, whereas no such behavior has been observed in LP1 and LP2 composites due to the very low concentration of PZT. For further confirmation about the formation of composite, LP20 (0.8LSMO-0.2PZT) was made. Refinement of X-ray diffraction pattern of LP20 and PZT are shown in Fig. 1(b) for comparison. Refinement of XRD pattern of LP20 system clearly shows the presence of LSMO and PZT without any intermediate phase (Fig. 1(b)). To verify the existence of PZT and formation of composite, scanning electron microscopy (SEM) and energy-dispersive X-ray spectroscopy (EDX) have been applied on LP5 and LP20. Figure 2(a) and 2(b) show the SEM images (EDX spectra in the inset) of LP5 and LP20 respectively. SEM images which show two different colors viz. black corresponds to LSMO and white corresponds to PZT signifies the presence of two different domains of LSMO and PZT respectively in the composites. The EDX analysis

confirms the presence of PZT in LP20 samples. It is worthy to point out here that the composition of the composites has only been demonstrated experimentally for the LP20 sample. The other composites have too small a concentration of the PZT dopant to be detected by XRD (Fig. 1a) or by EDX (Fig. 2a). The average particle size of LSMO, PZT and (1-x)LSMO-(x)PZT ($0.01 \leq x \leq 0.05$) nanocomposites estimated by using the Debye–Scherrer's formula[34,35] are ranging between 24 - 28 nm respectively.

The morphology and the microstructure of the nanocomposites have been examined by transmission electron microscopy (TEM). A typical TEM image of several nanoparticles of LP5 composite has been presented in Fig. 3(a). The closer look of Fig. 3(a) of different parts of the sample indicates that most of the nanoparticles are more or less spherical in shape and smooth in surface. Fig. 3(a) also shows that the grains are nanosized and have free surfaces of grain boundaries which should affect the magnetic properties.[15,16] The average particle size obtained from TEM measurements (~28 nm) matches well with the size estimated from the XRD study. Fig. 3(b) shows the HRTEM image of a single particle of the LP5 nanocomposite. The HRTEM micrograph shows two different interplanar spacing (*d*-value) of 0.277 nm and 0.414 nm which have been recognized as (110) plane of $La_{0.7}Sr_{0.3}MnO_3$ and (001) plane of $PbZr_{0.52}Ti_{0.48}O_3$ respectively. This confirms the co-existence of two phases in the composite. The patterns of planes indicate that all the nanoparticles are single crystalline in nature and free from major lattice defects.

Figs. 4(a) and 4(b) show the variation of magnetization with magnetic field (M-H) of the nanocomposites measured at room temperature (300 K) and low temperature (80 K) respectively. The M-H curves of LSMO-PZT composites at 300K and 80K indicate that the magnetization of the samples increases rapidly at low fields and then tends to saturate at higher field as shown in Fig. 4(a) and 4(b). The value of the magnetization of the composites decreases with PZT concentration (x). The saturation magnetization (M_S) obtained from M-H hysteresis curve measured at room temperature (300 K) and at low temperature (80 K) decreases with increase of PZT content in LSMO-PZT nanocomposites. Again this decrement remains more or less constant in both the temperatures (viz. 80 K and 300 K) as shown in the Table 1. Similar results were reported by Kanamadi et al.[36] in $CoFe_2O_4$-$Ba_{0.8}Sr_{0.2}TiO_3$ composite system. In the present system,

the magnetization in LSMO is due to the fact that the individual LSMO grains acts as centres of magnetization. In the composites when non-magnetic ferroelectric material (PZT) is incorporated into the manganite phase, it breaks the magnetic circuit. This results in decrease of magnetic parameters with increasing ferroelectric concentration in the composite. The left inset of Fig. 4(a) shows an enlarged view of the M-H curves, which confirms small coercivity viz. $H_C \approx 0.0123$ T for LP0 composite. The coercivity value has been verified also from dM/dH vs. H curve [right inset of Fig. 4(a) and 4(b)] which show the butterfly nature for all the nanocomposites. The values of the coercivity obtained from this plot are exactly same as obtained from the M vs. H plot. It should be pointed out that the coercivity does not vary appreciably with the variation of PZT concentration. Again, the magnetic transition in LSMO is observed due to percolation of ferromagnetic phases in paramagnetic matrix.[37] As the temperature increases the volume of ferromagnetic phases decrease and at a temperature the percolation between ferromagnetic phases becomes lost and ferromagnetic to paramagnetic transition occurs. Very recently, it has also been reported that the coercivity changes by changing the ferromagnetic correlation in LCMO.[38] In accordance with the facts[36,38] in the present investigation, due to the doping of small concentration of PZT (maximum 5%), the ferromagnetic domains do not move far away from each other. As a matter of fact the cooperation between ferromagnetic domains remains unchanged which in effect does not change the coercivity for the low concentration of PZT. It should be pointed out here that Kanamadi et al.[36] observed to decrease the coercivity with increase in $Ba_{0.8}Sr_{0.2}TiO_3$ in the high concentration regime of $Ba_{0.8}Sr_{0.2}TiO_3$ (~55%). In other words, addition of small concentration (up to 5%) of PZT (nonmagnetic material) in the present composite system does not affect the intrinsic property of LSMO.

Fig. 4(b) shows clear S-shape saturated open loop M-H curves for the nanocomposites measured at 80K. The coercivity measured from both the insets (viz. left and right) of Fig. 4(b) gives higher value ($H_C \approx 0.0142$T for LP0), which confirms that the super-paramagnetic phase disappears in low temperature region and system behaves as pure ferromagnetic.

One can estimate the particle size (d) by using the following relations[39]

$$V = 25\frac{k_B T_B}{K_u} \qquad (1)$$

Considering spherical particles $V = \frac{4}{3}\pi r^3$ and d=2r

where, V is the particle volume, r is particle radius, k_B is Boltzmann constant, T_B is blocking temperature and K_u the uniaxial anisotropy constant. The uniaxial anisotropy constant is related to maximum coercivity by the relation:

$$H_c = \frac{2K_u}{M_s} \quad (2)$$

where, M_s is the saturation magnetization. Since the superparamagnetic particles are spherical in shape as observed in TEM images, the average particle size of all LSMO-PZT composites were found to be about 30nm. This result corroborates the results obtained from XRD and TEM measurements.

The magnetic moment per formula unit (n_B) in Bohr magneton has been calculated by using the following relation,[40]

$$n_B = \frac{M \times M_s}{5585} \quad (3)$$

where,Mis the molecular weight of particular composition and M_s is saturation magnetization (emu/gm). It has been observed that n_B decreases from 2.069 μ_B to 1.692 μ_B at 80K and from 0.892 μ_B to 0.816 μ_B at 300K as PZT concentration increases from 1% to 5%. This may be due to the fact that when PZT concentration is increased in LSMO the molecular weight and saturation magnetization decreases.

Fig. 5(a) shows temperature variation of the dc magnetization of zero-field-cooled (ZFC) and field-cooled (FC) measurements for LSMO-PZT nanocomposites at a field of 100 Oe. The first measurement was taken after zero-field cooling (ZFC) at H=0 to the lowest temperature possible (175 K) and in the second run the measurements were taken under field cooled (FC) conditions (H=100 Oe). It has been observed from Fig. 5(a) that the superimposition (bifurcation) of the ZFC and FC curves take place at a certain temperature (T_S), which is different for different samples (LP1, LP2 and LP5). The superimposition of ZFC and FC curve is a characteristic property of superparamagnetic system.[41] The superparamagnetism induces in the system when the system changes from multi-domain to uniformly magnetized single domain. The interaction takes place among

these single domains of different nanoparticles and overall system is then in a state of uniform magnetization by changing from ferromagnetic to superparamagnetic phase which behaves like a small permanent magnet.[42] Superparamagnetism occurs due to single domain structure of magnetic LSMO nanoparticles. An increase in T_S (towards the higher temperature) has been observed with increase in PZT concentration. This is because the interaction between the single domain decreases by decreasing the superparamagnetic region and the bifurcation of ZFC and FC curve starts to occur at higher temperature. M-T curve exhibits characteristic ferromagnetic behavior for all LSMO-PZT nanocomposites. All the samples show paramagnetic to ferromagnetic transition at Curie temperature (T_c). The transition temperature (T_c) has been estimated as 360 K from the minimum obtained in dM/dT vs. T curves of FC plot [Fig. 5(b)] for all LSMO-PZT nanocomposites. These values are comparable to the values available in the literature.[22] The transition temperature does not change with PZT concentration because PZT does not interact with LSMO and occupies the interface or grain boundary of LSMO. The intrinsic property of LSMO remains unmodified. However, the non-magnetic PZT affects the extrinsic response which is evident from decrease in overall magnetic response (i.e magnetization) of the composite system.

Magnetic entropy change (ΔS_m) resulting from magnetic ordering has been calculated by using the equation:[43]

$$\Delta S_m = \int_o^{H_{max}} \frac{dM}{dT}(\Delta H) \qquad (4)$$

The variation of $\Delta S_m$with temperature is similar to that of dM/dT and observed values of ΔS_mat field H_{max}=100 Oe are 0.40, 0.35 and 0.25 $mJKg^{-1}K^{-1}$ for LP1, LP2 and LP5 respectively (see Table 1). This decrease in ΔS_m is attributed due to decrease in superparamagnetic nature of LSMO composites on addition of PZT which has also confirmed by the low temperature M-H plots.

The effect of PZT on the electrical transport property of LSMO-PZT composites has been studied from variation of the resistivity with the temperature. The variation of the resistivity with the temperature in the range from 50 K to 300 K is shown in Fig. 6. Nanophasic $La_{0.7}Sr_{0.3}MnO_3$ (LP0) system shows insulator to metal transition temperature (T_{IM}) at around 275 K below of which $La_{0.7}Sr_{0.3}MnO_3$ shows metallic behavior. With increasing PZT concentration (x), the zero-field (magnetic) resistivity of the LSMO–PZT

composites increases and the insulator–metal transition temperature (T_{IM}) shifts towards lower temperatures successively. It has been observed from Fig. 6 that insulator–metal transition temperature (T_{IM}) decreases drastically from 275 K to 165 K for the composite of 1% of PZT and with further increase of PZT concentration T_{IM} does not change significantly. The insulator–metal transition temperatures (T_{IM}) have been measured at 162 and 164 K for x = 0.02 and 0.05 respectively. These values are much lower than the value of $T_{IM} \sim 275$ K observed for pure LSMO. The resistivity of the composites has been increased with increasing PZT concentration. The different electrical transport behaviors and high resistivity of the composites should be related to the effect of dopant (PZT) on the electron transport channel in the composites.[44] In pure LSMO, the electrical transport is achieved through a direct contact between LSMO grains. However, in doped composites, there are two kinds of conduction channels connected parallel to each other.[45,46]. One is related to LSMO grains that determines the transport properties of the system through direct contact between LSMO grains. The other is related to dopants PZT. Since the dopant PZT has been segregated at the grain boundaries and on the surface of LSMO grains, the energy barriers and more scatterings are produced to electrical transport process giving rise to the higher resistivity observed for the doped composites. These results reported for other composites corroborates with this behavior.[47–49] The resistivity increased in an order of 10^2 as PZT concentration increased from 0% to 5%.

Conduction behavior in insulator region of the composite system has been studied. The curves of lnρ vs. $T^{-1/2}$ have been plotted for LP0, LP1, LP2 and LP5 in Fig.7. The resistivity for LP0, LP1, LP2 and LP5 shows linear dependence with $T^{-1/2}$ down to 274 K, 181 K, 177 K and 180 K respectively and after that insulator–metal transition occurs for each system. This study confirms that the conduction is dominantly governed by tunneling effect between magnetic phases[50] below the insulator–metal transition (i.e. in insulator region). Above the insulator–metal transition (i.e. in metallic region) all samples show deviation from $T^{-1/2}$ dependency, which indicates that some other mechanism is responsible for conduction in the metallic region. In the present system the resistivity in metallic region varies with $T^{1.5}$ (Fig. 8) in a broad temperature range (up to 180 K for LP0 and near 130 K for LP1-LP5). This result indicates non-Fermi liquid behavior dominates in metallic phases, which have been reported for other metallic ferromagnetic materials.[51-53]. It should be pointed out that simultaneous occurrence of the two phase transitions (viz.

paramagnetic-ferromagnetic transition and metal-insulator transition) in $La_{0.7}Sr_{0.3}MnO_3$ is due to the co-existence of two phases: viz. ferromagnetic metallic phase (FMM) and anti-ferromagnetic insulating (AFMI) phase.[37] As the temperature decreases the FMM phase increases in expense of AFMI phase. Therefore, both transitions (magnetic and I-M) occur simultaneously.

The field dependence of magnetoresistance (%MR) for LP0, LP1, LP2 and LP5 nanocomposites at 200K and that for LP5 at different temperatures (100, 150, 200 and 250 K) are shown in Fig. 9. The MR is defined as:

$$\Delta R/R = (R_H - R_0)/R_0 \quad (5)$$

where, R_H and R_0 are the resistances with and without a magnetic field (H). The results confirm that the MR for all nanocomposites decreases continuously with decreasing temperature. This behavior for a typical composite LP5 is shown in the inset of Fig. 9. The max MR (33%) has been observed for LP5 among all composites with the field 2800 Gauss at 200K (Fig. 7). Magnetoresistance (MR) of the composites is observed in a wide range of temperature (300K to 100K) below the ferromagnetic transitions (i.e. 360K). MR originates from the spin fluctuation within grains[54] and from spin-dependent scattering of polarized electrons at the grain boundaries (GBs).[55] Therefore, this large variation in the MR at low temperature in LSMO-PZT nanocomposite is due to the effect of the large spin polarization and pinning of domain walls at the GBs.[56,57] Values of MR for LSMO-PZT nanocomposites are 3-8% higher than that of pure LSMO indicating that the effect on MR is more pronounced in presence of PZT. MR decreases linearly with increasing field up to 500 Gauss for all temperatures, implies reorientation of the magnetic moments towards the magnetic field in the grains. At larger fields, the MR for the composite tends towards saturation. This result reflects the electrical and magnetic properties of the grains and is related to the field induced magnetic ordering of the spins at the surface layer of the grains. Inset of Fig. 6 confirms the increasing value of max MR (at 2800 Gauss) for LP5 with decrease in temperature and weak temperature dependence below ~ 250K.

Conclusion

The nanocomposites of LSMO-PZT have been successfully synthesized using sol-gel method. The results obtained from the Rietveld refinement of XRD and HRTEM analysis confirm the formation of the desired crystallographic phases of LSMO-PZT nanocomposites ($R\bar{3}c$ and P4mm space group) with interplanar spacing (*d*-value) of 0.277 nm and 0.414 nm for (110) plane of LSMO and (001) plane of PZT respectively. SEM and EDX studies confirm the formation of the composite. The average particle size of LSMO, PZT, and LSMO-PZT nanocomposites ranges between 24-30 nm as estimated from XRD, TEM, and magnetic measurements. The M-H analysis suggests that the saturation magnetization, shape of the hysteresis loops, the value of magnetic moment and the magnetic phase (transformation from superparamagnetic to ferromagnetic phase) have been modified in LSMO-PZT nanocomposites. Moreover, addition of small concentration (up to 5%) of PZT (nonmagnetic material) does not affect the intrinsic property of LSMO. The low temperature M-T studies confirm that the transition temperature remains unchanged at 360K with PZT concentration. It also exhibits decrease in entropy (ΔS_m) of LSMO nanoparticles on addition of PZT. Electrical measurements show a rapid decrease in the insulator– metal transition temperature (T_{IM}) with addition of small amount of PZT and then remain almost constant with higher concentration of PZT. All samples show $T^{-1/2}$ dependence of resistivity in the insulator region and $T^{1.5}$ dependence in the metallic region. This implies that the conduction in the insulator region is governed by tunneling between magnetic phases and the conduction shows non-Fermi liquid behavior in the metallic region. MR value decreases with decrease in temperature. The MR shows the lowest value at 100K for LP5. Variation in the MR at low temperature in LSMO-PZT nanocomposite is due to the effect of the large spin polarization and pinning of domain walls at the GBs.

Acknowledgements

A.K.G. is thankful to DST and DAE-BRNS, India for financial supports (Grant No.: SR/S2/CMP-0038/2008) and (Grant No.: 2011/37P/11/BRNS/1038-1) respectively.

References

1 S. Jin, T. H. Tiefel, M. McCormack, R. A. Fastnascht, R. Ramesh and L. H. Chen, *Science*, 1994, **264,** 413-415.

2 J. Z. Sun, W. J. Gallagher, P. R. Duncombe, L. Krusin-Elbaum, R. A. Altman, A. Gupta, Y. Lu, G. Q. Gong and G. Xiao, *Appl. Phys. Lett.*, 1996, **69**, 3266-3268.

3 M. Imada, A. Fujimori and Y.Tokura, *Rev. Mod. Phys.*, 1998, **70**, 1039-1263.

4 A. J. Millis, *Nature (London)*, 1998, **392,** 147-150.

5 A. Urushibara, Y. Moritomo, T. Arima, A. Asamitsu, G. Kidon and Y. Tokura, *Phys. Rev. B: Condens. Matter Mater. Phys.*, 1995, **51,** 14103-14109.

6 J. S. Zhou and J. B. Goodenough, *Phys. Rev. B: Condens. Matter Mater. Phys.*, 2001, **64**, 024421.

7 C. Zener, *Phys. Rev.*, 1951, **82**, 403-405.

8 P. W. Anderson and H. Hasegawa, *Phys. Rev.*, 1955, **100**, 675-681.

9 P. G. de Gennes, *Phys. Rev.*, 1955, **100**, 564-573; K. Kubo and N. Ohata, *J. Phys. Soc. Jpn.*, 1972, **33**, 21-32.

10 N. Furukawa, *J. Phys. Soc. Jpn.*, 1995, **64**, 3164-3167.

11 M. Jaime, P. Lin, M. B. Salamon and P. D. Han, *Phys. Rev. B: Condens. Matter Mater. Phys.*, 1998, **58**, R5901-R5904.

12 A. P. Ramirez, *J. Phys.: Condens. Matter*, 1997, **9**, 8171-8199.

13 W. Archiald, J. S. Zhou and J. B. Goodenough, *Phys. Rev. B: Condens. Matter Mater. Phys.*, 1996, **53,** 14445-14449.

14 A. J. Millis, P. B. Littlewood and B. I. Shraiman, *Phys. Rev. Lett.*, 1995, **74**, 5144-5147.

15 A. J. Millis, *Phys. Rev. B: Condens. Matter Mater. Phys.*, 1996, **53**, 8434-8441.

16 Y-H Huang, C-H Yan, Z-M Wang, C-S Liao and G-X Xu, *Solid State Commun.*, 2001, **118** 541-546.

17 B. B. Straumal, A. A. Mazilkin, S. G. Protasova, P. B. Straumal, A. A. Myatiev, G. Schütz, E. J. Goering, T. Tietze and B. Baretzky, *Philos. Mag.*, 2013, **93**, 1371-1383.

18 Shiv Kumar, S. Basu, B. Rana, A. Barman, S. Chatterjee, S. N. Jha, D. Bhattacharyya, N. K. Sahoo and Anup K.Ghosh, *J. Mater. Chem. C*, 2014, **2**, 481-495.

19 A. Gaur and G. D. Varma, *J. Phys.: Condens. Matter*, 2006, **18**, 8837-8846.

20 Y. Tokura, A. Urushihara, Y. Moritomo, T. Arima, A. Asamitsu, G. Kido and N. Furukwa, *J. Phys. Soc. Jpn.*, 1994, **63**, 3931-3935.

21 L. I. Balcells, I. R. Enrich, J. Mora, A. Calleja, J. Fontcuberta and X. Obradors, *Appl. Phys. Lett.*, 1996, **69**, 1486-1488.

22 P. Dutta, P. Dey and T. K. Nath, *J. Appl. Phys.*, 2007, **102**, 073906.

23 Z. F. Zi, Y. P. Sun, X. B. Zhu, Z. R. Yang, J. M. Dai and W. H. Song, *J. Magn. Magn. Mater.*, 2009, **321**, 2378-2381.

24 Q. A. Pankhurst, J. Connolly, S. K. Jones and L. Dobson, *J. Phys. D:App. Phys.*, 2003, **36**, R167-R181.

25 S. Vasseura, E. J. DuguetPortiera, G. Goglioa, S. Morneta, E. Hadova, K. Knizek, M. Marysko, P. Veverka and E. Pollert, *J. Magn. Magn. Mater.*, 2006, **302**, 315-320.

26 K. Zhang, T. Holloway, J. Pradhan, M. Bahoura, R. Bah, R. R. Rakhimov, A. K. Pradhan, R. Prabakaranand G. T. Ramesh, *J. Nanosci. Nanotechnol.*, 2010, **10**, 5520-5526.

27 A. K. Pradhan, R. Bah, R. B. Konda, R. Mundle, H. Mustafa, O. Bamiduro, R. R. Rakhimov, X. Wei and D. J. Sellmyer, *J. Appl. Phys.*, 2008, **103**, 07F704.

28 Y. S. Yoon, S. H. Kim, S. J. Lee, H. K. Kim and M. J. Lee, *Sens. Actuators A*, 2006, **125**, 463-470.

29 J. H. Kim, C. D. Kim, M. J. Kim, K. L. Ha and N. Chubachi, *Jpn. J. Appl. Phys. Part-1*, 2001, **40**, 3652-3653.

30 M. Schreiter, R. Gabl, D. Pitzer and W. Wersing, *J. Eur. Ceram. Soc.*, 2004, **24**, 1589-1592.

31 M. H. Kwak, S. E. Moon, S. J. Lee, Y. T. Kim, H. C. Ryu and W. J. Kim, *Integr. Ferroelectr.*, 2003, **54**, 659-664.

32 Kathrin Dorr, *J. Phys. D: Appl. Phys.*, 2006, **39**, R125–R150.

33 O. M. Hemeda, A. Tawfik, A. Al-Sharif, M. A. Amer, B. M. Kamal, D. E. El Refaay and M. Bououdina, *J. Magn. Magn. Mater.*, 2012, **324**, 4118-4126.

34 B. D. Cullity, *Elements of X-Ray Diffraction*, Addison-Wesley, MA.1978.

35 A. L. Patterson, *Phys. Rev.*, 1939, **56**, 972-977.

36 C.M. Kanamadi, B.K. Das, C.W Kim, D.I Kang, H.G Cha, E.S Ji, A.P. Jadhav, B.E Jun, J.H Jeong, B.C Choi, B.K. Chougule and Y.S Kang, *Mater. Chem. Phys*. 2009,**116**, 6–10.

37 E. Dagotto, Takashi Hotta and Adriana Moreo, *Physics Reports*, 2001, **344**, 1-153.

38 J.J. Neumeier and J.L. Cohn, *Phys. Rev. B: Condens. Matter Mater. Phys.*, 2000, **61**, 14319.

39 S. R. Shinde, S. B. Ogale, J. S. Higgins, H. Zheng, A. J. Millis, V. N. Kulkarni, R. Ramesh, R. L. Greene and T. Venkatesan, *Phys. Rev. Lett.*, 2004, **92**, 166601.

40 S. Singhal and K. Chandra, *J. Solid State Chem.*, 2007, **180**, 296-300.

41 T. J. Park, C. Georgia, Papaefthymiou, A. J. Viescas, A. R. Moodenbaugh and S. S. Wong, *Nano Lett.*, 2007, **7(3)**,766–772.

42 N. D. Thorat, K. P. Shinde, S. H. Pawar, K. C. Barick, C. A. Bettyc and R. S. Ningthoujam, *Dalton Trans.*, 2012, **41**, 3060-3071.

43 V. K. Pecharsky and K. A. Gschneidner Jr, *J. Appl. Phys.*, 2001, **90**, 4614-4622.

44 A. Gaur and G. D. Varma, *Solid State Commun.,* 2006, **139**, 310–314.

45 J.M. Rubinstein, J. Appl. Phys. 87 (2000) 5019.

46 A. de Andres, M. Garcia-Hernandez, J.L. Martinez, C. Prieto, *Appl. Phys. Lett.*, 74 (1999) 3884.

47 L. D. Yao, W. Zhang, J. S. Zhang, H. Yang, F. Y. Li, X. Liu, C. Q. Jin and R.C. Yu, *J. Appl. Phys.*, 2007, **101**, 063905.

48 Y. Dang-Hyok, K. Raju, M. Bong-Ki and P. V. Reddy, *Ceramics International*, 2014, **40**, 13497–13505.

49 W. J. Lu, Y. P. Sun, X. B. Zhu, W. H. Song and J. J. Du, *Materials Letters*, 2006, **60,** 3207–3211.

50 Y. H. Sun, Y. G. Zhao, M. H. Zhu, B. T. Xie and W. B. Wu, *J. Appl. Phys.,* 2012, **112**, 023908.

51 C. Pfleiderer, G. J. McMullan, S. R. Julian and G. G. Lonzarich, *Phys. Rev. B: Condens. Matter Mater. Phys.*, 1997, **55**, 8330-8338.

52 J. T. Rijssenbeek, R. Jin, Yu. Zadorozhny, Y. Liu, B. Batlogg and R. J. Cava, *Phys. Rev. B*, 1999, **59**, 4561-4564.

53 I. H. Inoue, I. Hase, Y. Aiura, A. Fujimori, Y. Haruyama, T. Maruyama and Y. Nishihara, *Phys. Rev. Lett.*, 1995, **74**, 2539-2542.

54 H.Y. Hwang, S.W. Cheong, N.P. Ong and B. Batlogg, *Phys. Rev. Lett.*, 1996, **77**, 2041.

55 M. Navasery, S.A. Halim, N.Soltani, G.Bahmanrokh, A.Dehzangi, M.Erfani H, A. Kamalianfar, S.K.Chen, and K.Y.Pan, *Int. J. Electrochem. Sci.,* 2013, **8**, 467 – 476.

56 L. Yan, L. B. Kong, T. Yang, W. C. Goh, C. Y. Tan, C. K. Ong, M. A. Rahman, T. Osipowicz and M. Q. Ren, *J. Appl. Phys.*, 2004, **96**, 1568-1571.

57 S. Kamba, D. Nuzhnyy, M. V. Savino, J. Sěbek, J. Petzelt, J. Prokleěka, R. Haumont and J. Kreisel, *Phys. Rev. B: Condens. Matter Mater. Phys.*, 2007, **75**, 024403-024408.

Figure Caption:

Fig. 1(a) Rietveld refined XRD pattern of (1-x) LSMO-x PZT (where x=0.00, 0.01, 0.02 and 0.05) nanocomposites; (b) Rietveld refined XRD pattern of PZT and 0.8 LSMO-0.2 PZT nanocomposite;.

Fig. 2 SEM image for LP5 (a) and for LP20 (b). Inset of each figure shows Energy-dispersive X-ray spectroscopy (EDX) pattern.

Fig. 3 (a) TEM and (b) HRTEM images of 0.95 LSMO-0.05 PZT nanocomposite.

Fig. 4 M-H hysteresis curves of (1-x) LSMO-(x) PZT nanocomposites (where x = 0.00, 0.01, 0.02 and 0.05) at (a) 300 K and (b) 80 K. Corresponding left insets of figures show extended view of M-H hysteresis and right insets of figures show dM/dH vs H curves in the range of -0.2 T to +0.2 T.

Fig. 5 (a) Zero Field Cooled (ZFC) and Field Cooled (FC) M-T curves, (b) dM/dT vs T curves of (1-x) LSMO-(x) PZT nanocomposites (where x = 0.01, 0.02 and 0.05) at 100 Oe.

Fig. 6 Temperature variation of resistivity of (1-x) LSMO-(x) PZT nanocomposites (where x =0.00, 0.01, 0.02 and 0.05).

Fig. 7 Variation of resistivity as function of $T^{-1/2}$ of (1-x) LSMO-(x) PZT nanocomposites (where x =0.00, 0.01, 0.02 and 0.05). Linear fit represents that the conduction is mainly due to tunneling between magnetic phases in metallic region.

Fig. 8 Variation of resistivity (ρ) as function of $T^{1.5}$ of (1-x) LSMO-(x) PZT nanocomposites (where x =0.00, 0.01, 0.02 and 0.05). Non-Fermi liquid behavior plays a major role for the conduction in metallic region.

Fig. 9 Variation of magneto-resistance (MR) with magnetic field (H) of different nanocomposites at 200 K. The inset of the figure shows variation of MR with magnetic field for LP5 nanocomposites at different temperatures.

TOC: (a) M-H hysteresis curves of nanocomposites 80 K. Insets of figure show extended view of M-H hysteresis (left) and dM/dH vs. H curves in the range of -0.2 T to +0.2 T (right); (b) Variation of magneto-resistance (MR) with magnetic field (H) of different nanocomposites at 200K. The inset of the figure shows variation of MR with magnetic field for a nanocomposite at different temperatures.

Table Caption:

Table 1. Variation of saturation magnetization (M_s), coercivity (H_c) and magnetic moment (n_B) at 300K and 80K; the variation of entropy for LP1, LP2 and LP5 nanocomposites:

Table 1. Variation of saturation magnetization (M_s), coercivity (H_c) and magnetic moment (n_B) at 300K and 80K; the variation of entropy for LP1, LP2 and LP5 nanocomposites:

LSMO-PZT composites	300K			80K			ΔS ($mJKg^{-1}K^{-1}$)
	M_s (emu/gm)	H_c (T)	n_B (μ_B)	M_s (emu/gm)	H_c (T)	n_B (μ_B)	
LP1	28.14	0.0123	0.892	48.89	0.0142	2.069	0.40
LP2	21.09	-do-	0.873	38.34	-do-	1.927	0.35
LP5	16.52	-do-	0.816	34.24	-do-	1.692	0.25

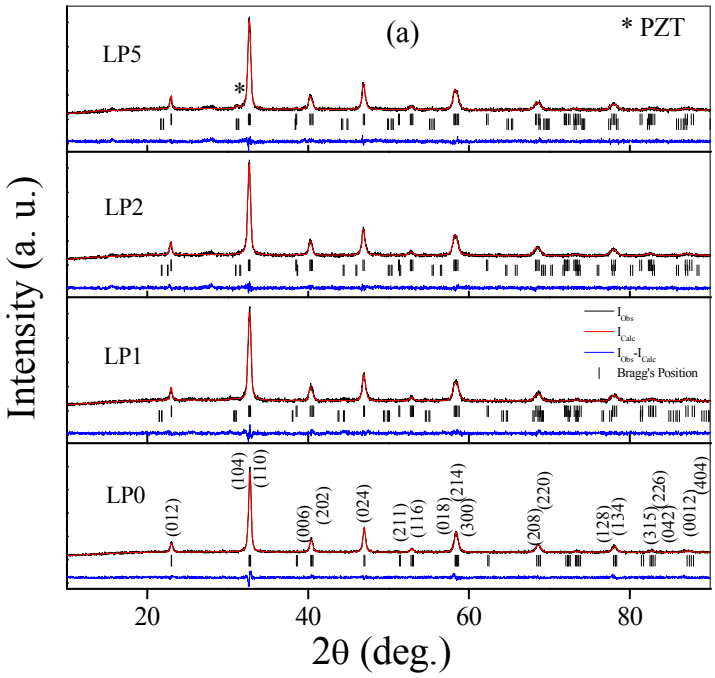

Fig. 1(a)

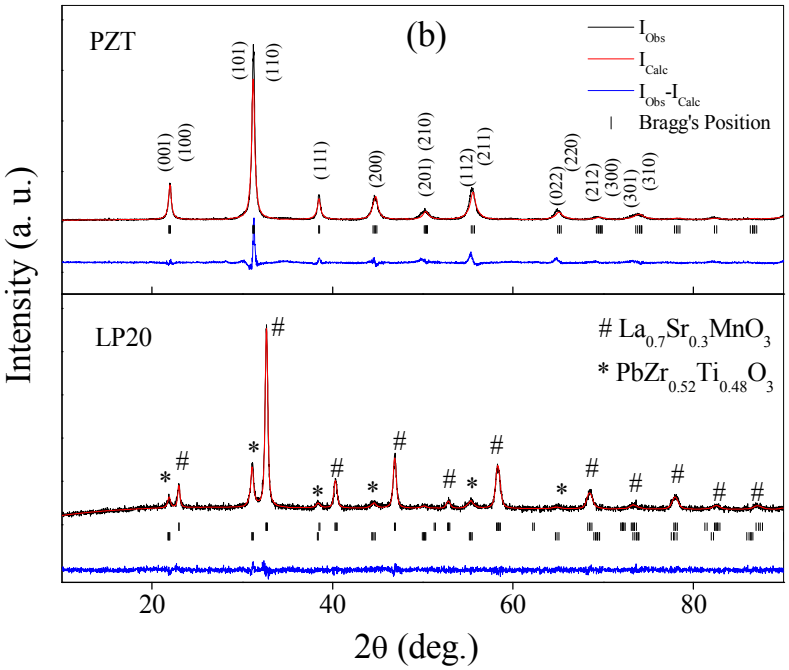

Fig. 1(b)

Fig. 1(a) Rietveld refined XRD pattern of (1-x) LSMO-x PZT (where x=0.00, 0.01, 0.02 and 0.05) nanocomposites; (b) Rietveld refined XRD pattern of PZT and 0.8 LSMO-0.2 PZT nanocomposite.

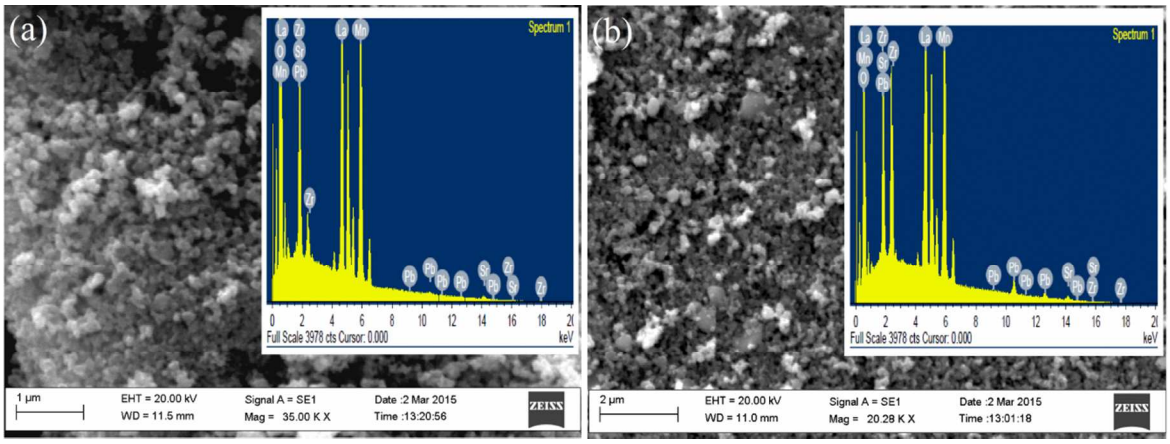

1

Fig. 2

Fig. 2 SEM image for LP5 (a) and for LP20 (b). Inset of each figure shows Energy-dispersive X-ray spectroscopy (EDX) pattern.

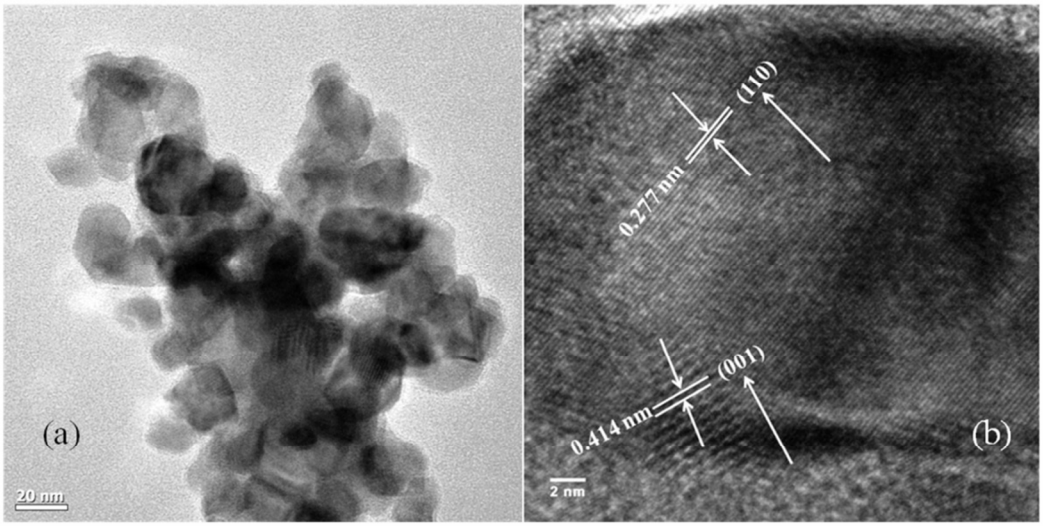

Fig. 3 (a) TEM and (b) HRTEM images of 0.95 LSMO-0.05 PZT nanocomposite.

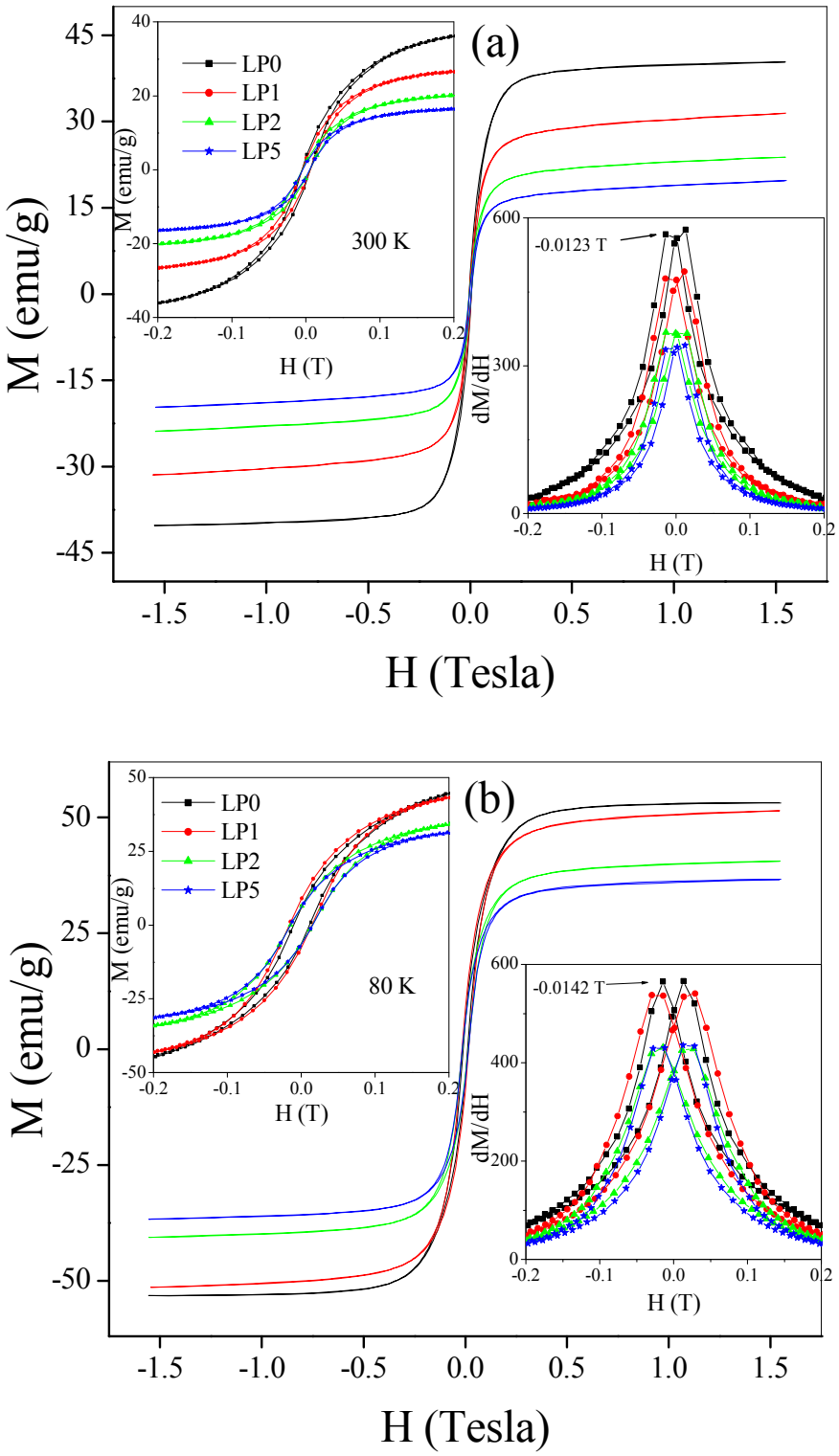

Fig. 4 M-H hysteresis curves of (1-x) LSMO-(x) PZT nanocomposites (where x = 0.00, 0.01, 0.02 and 0.05) at (a) 300 K and (b) 80 K. Corresponding left insets of figures show extended view of M-H hysteresis and right insets of figures show dM/dH vs H curves in the range of -0.2 T to +0.2 T.

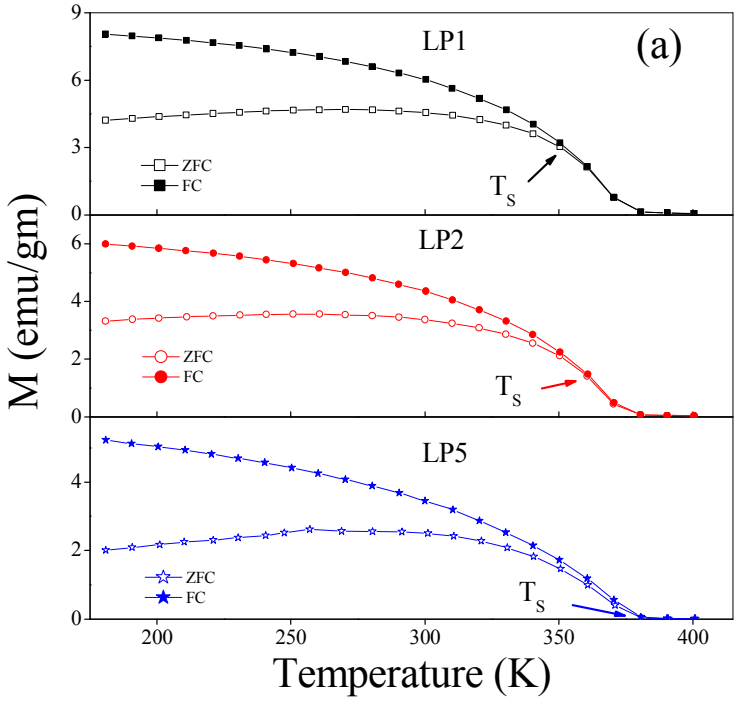

Fig. 4(a)

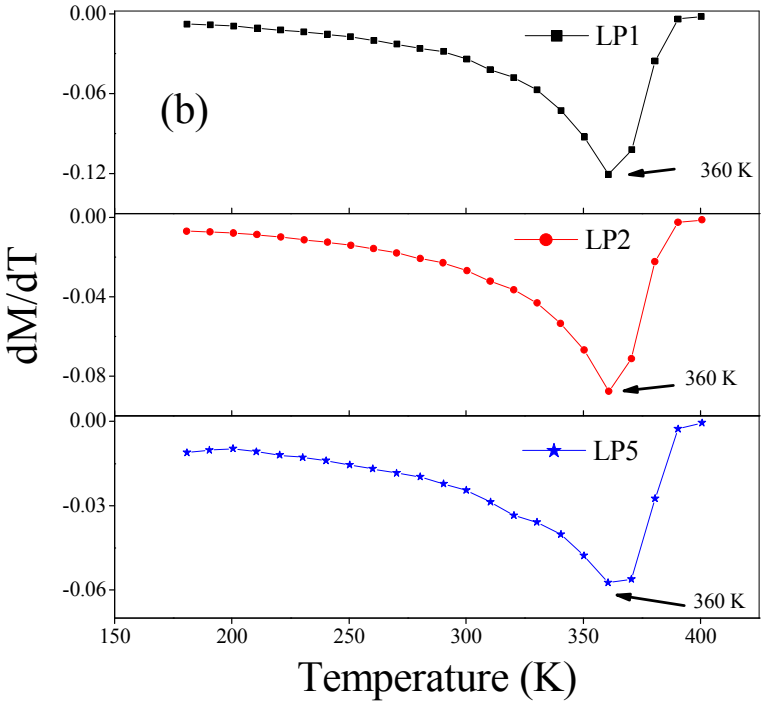

Fig. 5 (a) Zero Field Cooled (ZFC) and Field Cooled (FC) M-T curves, (b) dM/dT vs T curves of (1-x) LSMO-(x) PZT nanocomposites (where x = 0.01, 0.02 and 0.05) at 100 Oe.

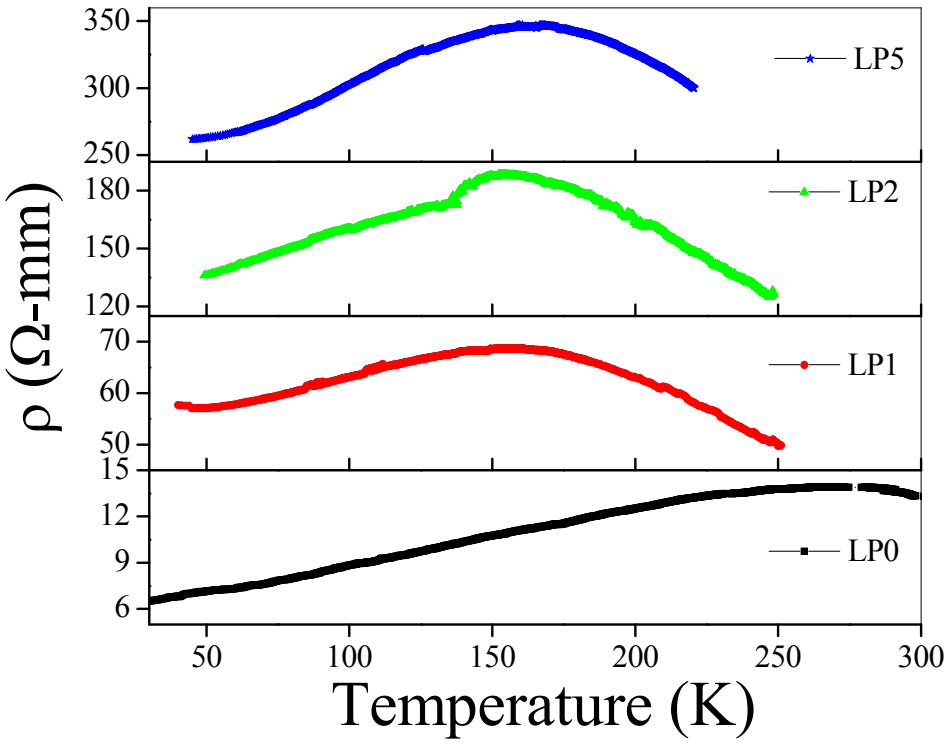

Fig. 6 Temperature variation of resistivity of (1-x) LSMO-(x) PZT nanocomposites (where x =0.00, 0.01, 0.02 and 0.05).

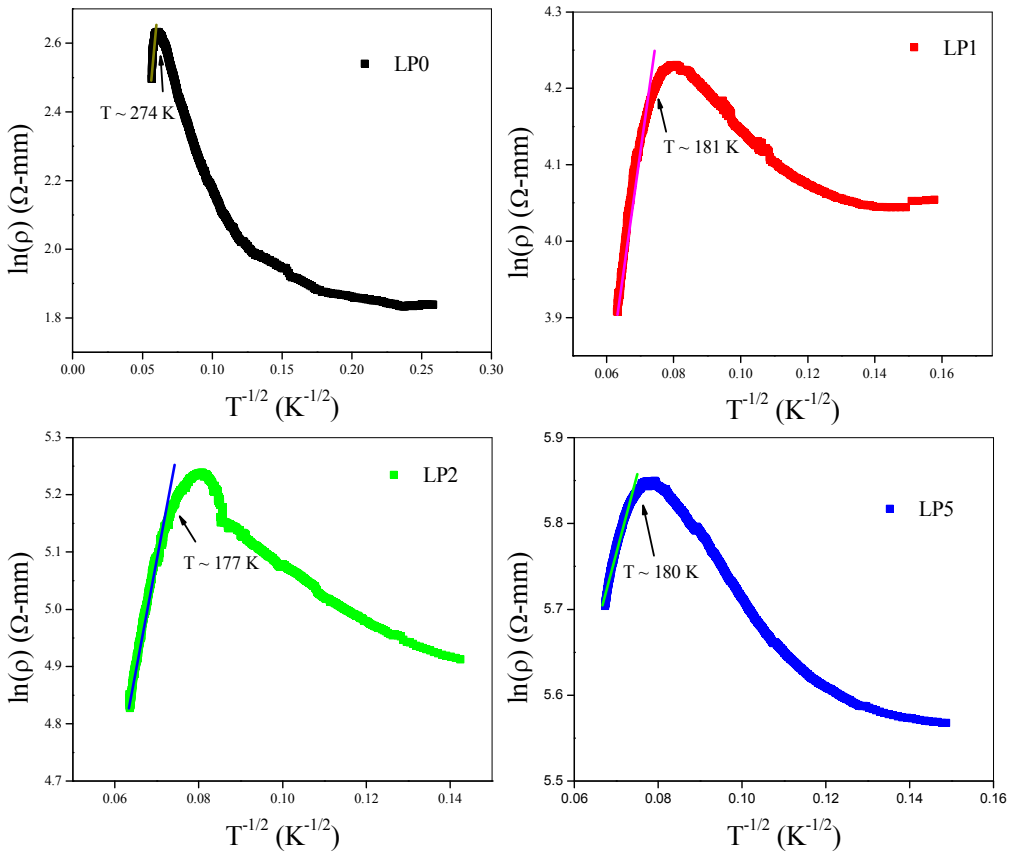

Fig. 7 Variation of resistivity as function of $T^{-1/2}$ of (1-x) LSMO-(x) PZT nanocomposites (where x =0.00, 0.01, 0.02 and 0.05). Linear fit represents that the conduction is mainly due to tunneling between magnetic phases in metallic region.

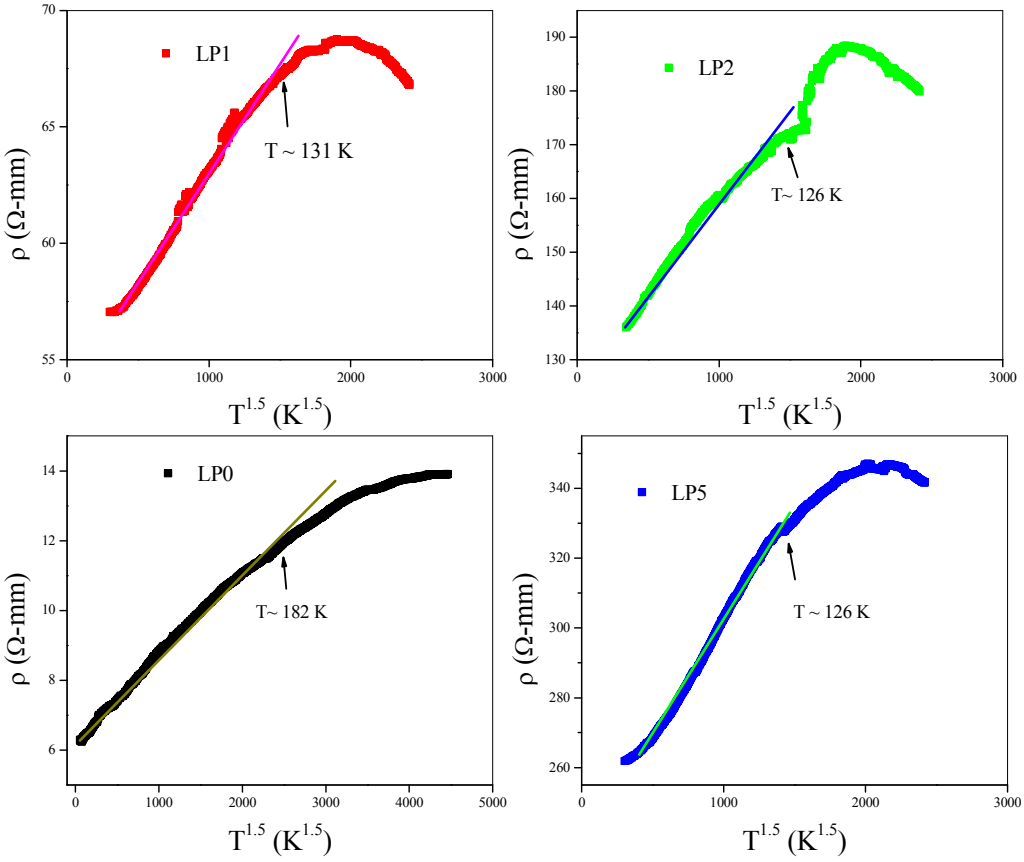

Fig. 8 Variation of resistivity (ρ) as function of $T^{1.5}$ of (1-x) LSMO-(x) PZT nanocomposites (where x =0.00, 0.01, 0.02 and 0.05). Non-Fermi liquid behavior plays a major role for the conduction in metallic region.

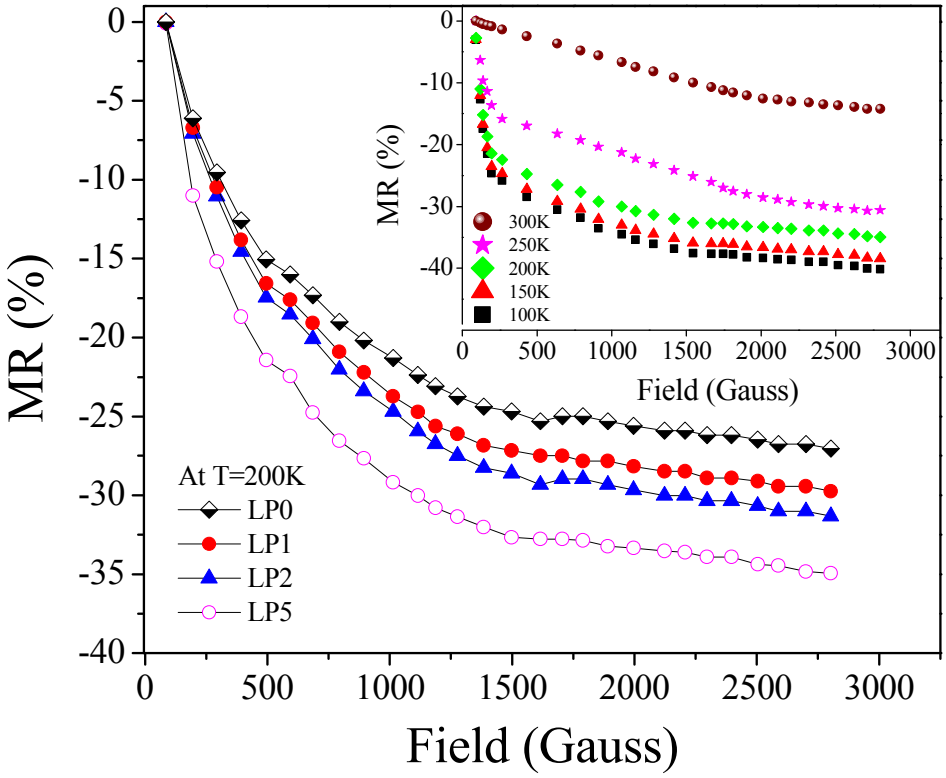

Fig. 9 Variation of magneto-resistance (MR) with magnetic field (H) of different nanocomposites at 200 K. The inset of the figure shows variation of MR with magnetic field for LP5 nanocomposite at different temperatures.